Star Formation in the HII Regions RCW 38, RCW 36, and RCW 108

Miquela Vigil

MIT Dept of Earth, Atmospheric, and Planetary Science

June 2004

The author hereby grants to MIT permission to reproduce and to distribute publicly paper and electronic copies of this thesis document in whole or in part

Copyright © Miquela C. Vigil. All rights reserved.

Submitted to the Department of Earth, Atmospheric, and Planetary Science in partial fulfillment of the requirements for the degree of Masters of Science in Earth, Atmospheric, and Planetary Science at the Massachusetts Institute of Technology

Signature of Author _____
Miquela C. Vigil

Certified by _____
Scott Wolk
Harvard/Smithsonian Center for Astrophysics
Thesis Advisor

Certified by _____
Tyler Bourke
Harvard/Smithsonian Center for Astrophysics
Thesis Advisor

Accepted by _____
Maria Zuber
E.A. Griswold Professor of Geophysics
Department Head

MASSACHUSETTS INSTITUTE OF TECHNOLOGY
AUG 2 5 2004
LIBRARIES

ARCHIVES

ABSTRACT

I present 1.2 mm observations of the HII regions RCW 38, RCW 36, and RCW 108 which reveal the distributions of dust associated with the three regions. The dust emission in RCW 38 exhibits a ring like structure centered around an O-star. A bright knot in the ring was determined to contain 15% of the total dust by mass in the region and roughly coincided with regions of high emission at various infrared wavelengths as well as 6 cm continuum emission. The dust emission in RCW 36 extended along a ridge with a bright clump in the north of the ridge containing 70% of the mass of the entire cluster. The dust emission in RCW 108 is concentrated in a single tight knot with a faint extension to the south. The dust emission is compared to the infrared and radio emissions to attempt to describe the characteristics of possible areas of active star formation.

1. Introduction

1.1. Star Formation and the Interstellar Medium

Star formation occurs in the dense cores of molecular clouds. Young stellar clusters embedded within these molecular clouds provide key information, such as the inital mass function, about the process of star formation in galaxies. Embedded clusters are either fully or partially surrounded by interstellar gas and dust which causes them to be difficult to detect at optical wavelengths and easiest to detect in the infrared and longer wavelengths, e.g., millimeter and centimeter wavelengths.

The model for the formation of low mass stars (Shu, Adams, & Lizano 1987; Shu et al. 1993) begins with a dense core where the core slowly condenses until the central region becomes unstable to gravitational collapse. In this state, the thermal pressure is the only

force counteracting the self-gravity of the core. The core then undergoes free-fall collapse. After collapse, three evolutionary stages follow: 1.) an accretion stage which involves a protostar and circumstellar disk surrounded by in-falling gas and dust; 2.) a stage in which the protostar transfers momentum, angular and linear, to its surroundings through jets and molecular outflows; and 3.) a stage where the protostar becomes optically visible and then enters the zero age main sequence, decreasing its luminosity.

Massive stars produce significant output of UV photons and strong winds which can have appreciable effects on the surrounding medium. The UV photons will ionize the surrounding gas while the winds can push out gas and dust from the surroundings. This region of ionized hydrogen is known as an HII region. The effects on the surroundings can possibly trigger further star formation in nearby regions, but may also curb star formation in the immediate vicinity due to the excavation of dust and gas by winds from newly formed stars.

The surrounding environment of embedded clusters changes with the evolution of the cluster. The youngest clusters are usually partially or fully embedded within the cold dense molecular material of the core, while the older, more evolved clusters are surrounded by hot dusty regions of ionized hydrogen. Studies of these clusters at different stages in their evolution allow us to construct a picture of the process of star formation.

1.2. HII Regions

Hydrogen atoms in the interstellar medium can be ionized by ultraviolet radiation from young, hot stars creating regions called HII regions. HII regions are created by massive, bright and short-lived stars which are as massive as 20-100 solar masses but are more luminous than 10000 Suns. They die in supernovae explosions and their lifetimes

are typically on the order of 10 million years. Designated as OB stars, these bright stars are typical tracers of star forming regions. Most stars form in clusters but OB stars are particularly useful because they are extremely bright making it possible to detect them from great distances.

The gas temperature of HII regions is typically between 5000-10000K and the average number densities are in the range of 100-10000 particles per cubic centimeter (Murdin 2001). Compared to terrestrial conditions, HII regions are very hot and dilute regions.

1.3. RCW 38

The southern HII region RCW 38 (Rodgers, Campbell & Whiteoak, 1960) is a young, massive embedded stellar cluster containing an early O star, designated IRS2 (Frogel & Persson 1974), clustered within hundreds of lower mass stars (Ligori et al. 1994; S. J. Wolk et al. 2004, in prep). RCW 38 is at a distance of 1.7 kpc (Muzzio 1979), which makes it one of the closest star forming regions containing an early O-type star. These characteristics make it is a prime target for high resolution studies of an embedded massive cluster after the O star has completed its ultracompact HII (UCHII) region phase, but during the phase where it greatly influences its natal environment and the evolution of its low mass cluster members. Near infrared images taken with 2MASS and VLT images are shown in Figure 1.

Frogel and Persson (1974) studied the region at 10 μm and found the warm dust emission to follow a horse-shoe shape across a 1.8×1.8 arcmin^2 area, labeling the peak IRS1. From its near infrared (NIR) colors, assuming a distance of 1.5 kpc, they suggest that the brightest NIR source, IRS2, is an early O-star (specifically O4) having about 12.8 mag of visual extinction, or a group of later spectral type O stars. This is sufficient to account for the observed continuum emission at 5 GHz (Shaver & Goss 1970).

Furniss, Jennings, & Moorwood (1975) combined broad-band 40-350 μm measurements with the previous work of Frogel & Persson to provide an alternate suggestion for the spectral type of IRS2. Furniss et al. argue that an O4 star would supply more than enough luminosity to account for all the infrared luminosity and emit enough Ly photons to yield twice the observed radio flux, unless significant absorption by dust is occurring. Instead, they suggest IRS2 is an O5 star with little or no dust absorption of the continuum photons in the ionized region.

Observations of the region in Brackett-γ at 2.16 μm (Mizutani et al. 1987) find an electron temperature of 8000 K and emission consistent with an ionizing source of three O6 stars or a single O5 star plus a cluster of heavily obscured lower mass stars. NIR imaging and photometry of the region by Ligori et al. (1994) revealed the presence of a cluster of optically invisible young stellar objects embedded in the nebular emission. NIR Very Large Telescope (VLT) images reveal that the embedded cluster surrounding IRS2 contains a few hundred members within a few tenths of a parsec (Wolk et al. 2002; S. J. Wolk et al. 2004, in preparation).

Mid-infrared imaging and spectroscopy by Smith et al. (1999) provide further evidence that the ionizing source of the region is at least O5 or earlier. Through modeling of the ratio of emission lines at IRS1, the ionizing radiation field constrains the ionizing source to be between O4.5 and O5.5. Smith et al. also find that the region surrounding IRS2 is depleted of dust, suggesting the region can be explained in terms of a wind blown cavity, where winds from IRS2 have blown out the surrounding material.

Cheung et al. (1980) derive a very large extinction of $\sim$800 mag. from 1 mm observations. Combining this result with the NIR observations suggests that RCW 38 is an embedded blister HII region lying just inside the front edge of a giant molecular cloud.

Caswell & Haynes (1987) calculate an electron temperature to be $\sim$7500 K from the

H109α and H110α recombination lines, with an observed line width of $\sim$34 km s^{-1} in a 4$'$.4 beam.

Previous studies of RCW 38 with the Chandra X-ray Observatory (CXO) by Wolk et al. (2002) find diffuse X-ray emission which they model as synchrotron emission, a surprising result. The peak of the diffuse X-ray emission corresponds to a cavity in the diffuse infrared emission. The origin of the synchrotron emission remains a mystery. The CXO observations also detect a few hundred X-ray point sources, with many having counterparts in the NIR (S. J. Wolk et al. 2004, in preparation). Figure 2 shows X-ray contours over a near infrared image taken by the Very Large Telescope of RCW 38.

RCW 38 was previously imaged at 6 and 18 cm and the H107α recombination line with the Austrialia Telescope Compact Array (ATCA) (Vigil et al. in preparation) to study the molecular gas morphology and velocity distribution. The 6 and 18 cm emission is concentrated in a circular structure with an empty cavity containing the O star IRS2 seen in Figure 3. The emission within the ring is not uniform and contains several clumps, the most notable near the position of IRS1. Line emission is detected inside the cavity and generally within the cm ring of emission as seen in Figure 4. An electron temperature for the region was calculated for the ring of emission to be 7300 K and for the IRS1 clump 9900 K.

1.4. RCW 36

The southern region RCW 36 (Rodgers, Campbell & Whiteoak, 1960) is a bright optical and radio HII region found within a prominent dust lane. Figure 12 is a K-band 2MASS image in which the stellar population associated with the region can be viewed. The region contains a stellar cluster embedded in a molecular cloud.

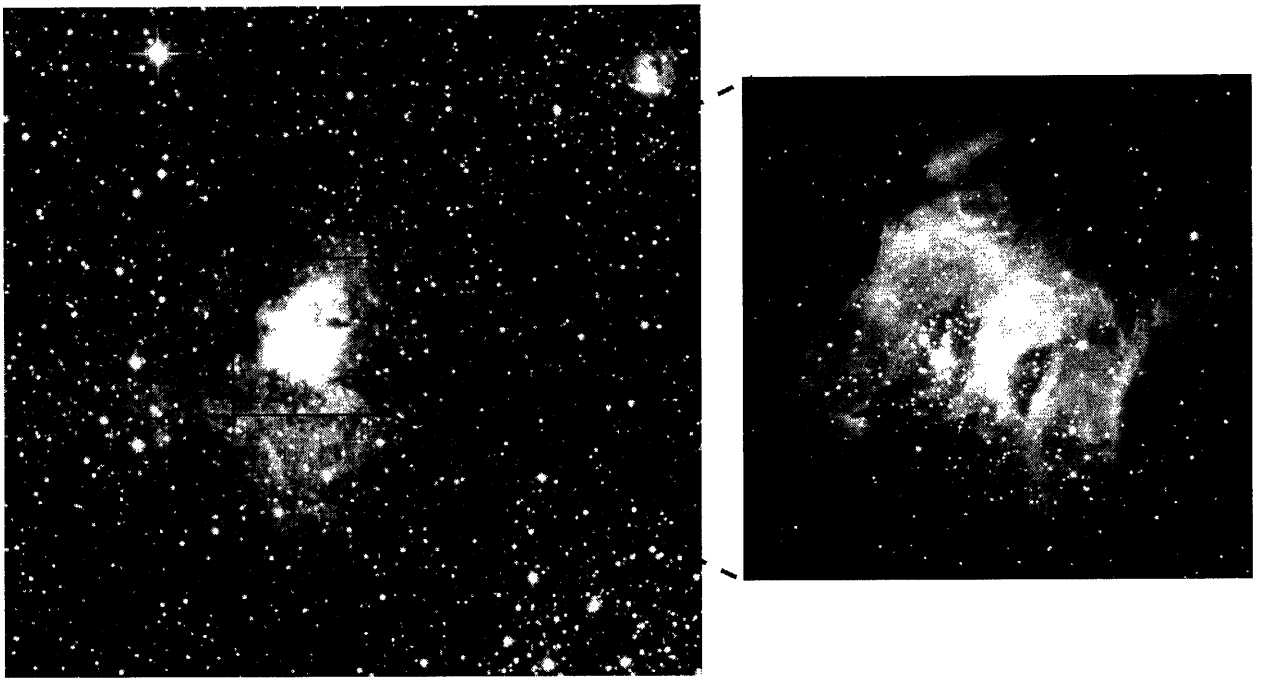

Fig. 1.— The image on the left was taken by the Two Micron All Sky Survey (2MASS) project and shows a 10′by 10′ region containing RCW 38. The image on the right was taken by the near infrared Very Large Telescope (VLT). It is approximately 2.5′by 2.5′ centered on IRS2. The bright ridge in the center contains the peak in the 10μm emission known as IRS1 (Frogel et al. 1974). The bright source to the east of the ridge is known as IRS2 and believed to be an O star (Frogel et al. 1974).

Several molecules associated with the RCW 36 have been detected. CO, H_2CO and OH have all been detected in the region by Brand et al. (1984), Gillespe et al. (1977), and Whiteoak and Gardner (1977) respectively.

An H_2O maser was also detected in the region by Braz and Scalise (1982). Some water molecules in star-forming regions can undergo population inversion resulting in the emission of radiation at 22 GHz. H_2O masers are good tracers of star formation. The H_2O maser labeled 265.151+1.454 is found near the continuum peak of RCW 36 at a position of RA(1950) 08h 57m 36.6s DEC(1950) -43° 33′38″. Further studies by Braz and Epchtein

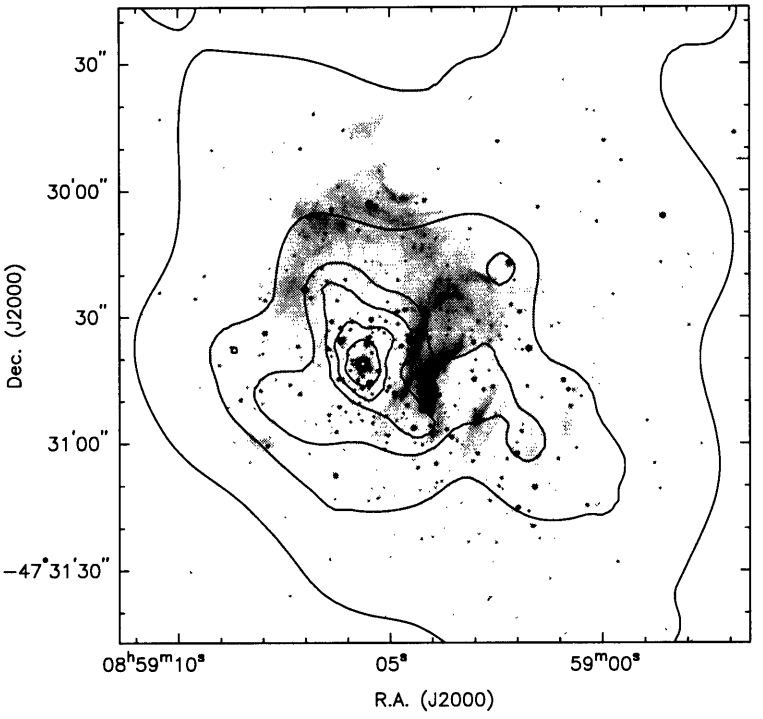

Fig. 2.— Diffuse X-ray contours overlaid on a K-band image taken with the VLT (Wolk 2004 in preparation). Contours represent 0.16, 0.4, 0.8, 1.6, 3 and 5 X-ray counts per pixel. The peak in the diffuse X-ray emission coincides with a cavity in the diffuse K-band emission. There also appears to be an interation between the diffuse X-ray gas and the bright ridge containing IRS2 as can be seen in the deformation of the contours around the ridge.

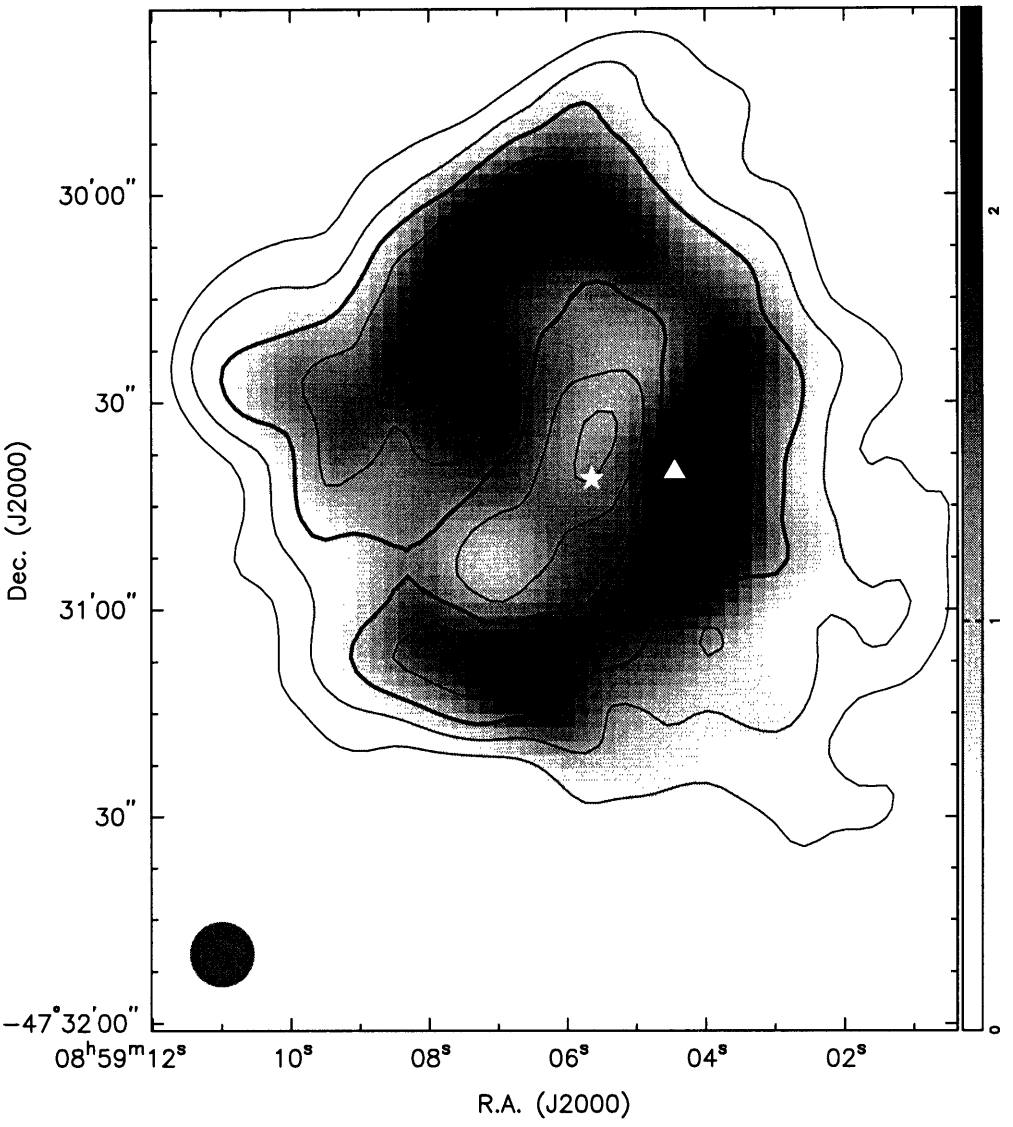

Fig. 3.— The underlying image is the 6 cm continuum image with 18 cm contours of RCW 38. The white triangle indicates the location of the peak at 10μm,IRS1, and the white star indicates the position of the O-star IRS2. The grey-scale intensity ranges linearly from 0 to 2.5 Jy beam^{-1}. The image was restored with a beam size of 10″ by 10″ shown in the lower left corner. The contours are 15, 30, 45, 60, 75, and 90% of the maximum flux of 3.501 Jy/beam. The bold contour marks the 60% contour.

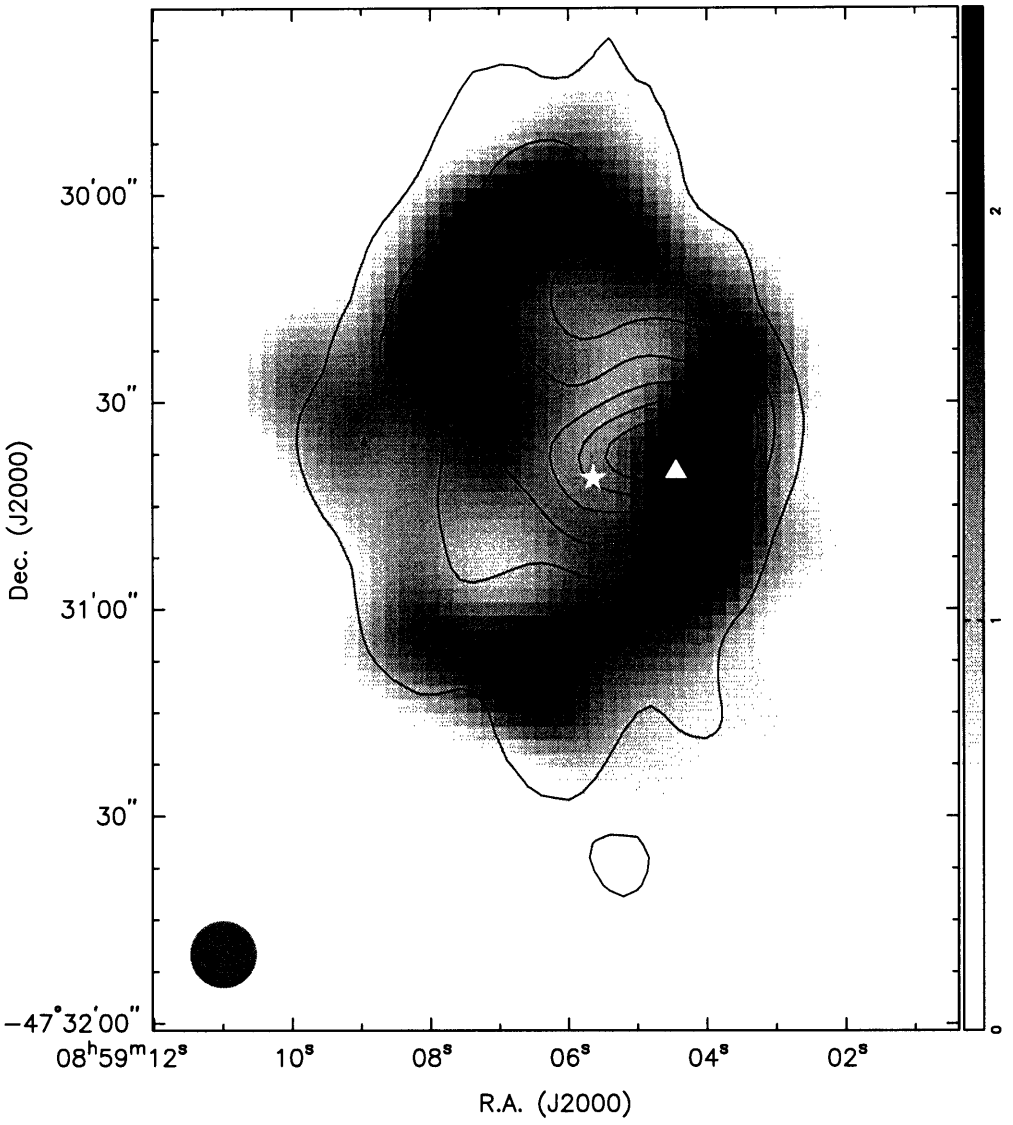

Fig. 4.— RCW 38 velocity integrated H107α line contours over 6 cm continuum grey-scale ranging from 0 to 2.5 Jy beam^{-1}. The restored beamsize is 10″ by 10″, shown in the lower left corner. The white star corresponds to the location of the O-star IRS 2 and the triangle marks the location of the 10μm peak IRS 1. The contour levels are 5, 20, 35, 50, 65, 80, and 95 percent of the peak intensity of 0.266 Jy/beam.

(1982) at 2.2 μm revealed 5 near-infrared sources in the vicinity of the maser. The source closest to the radio continuum peak was interpreted as the excitation star of the HII region

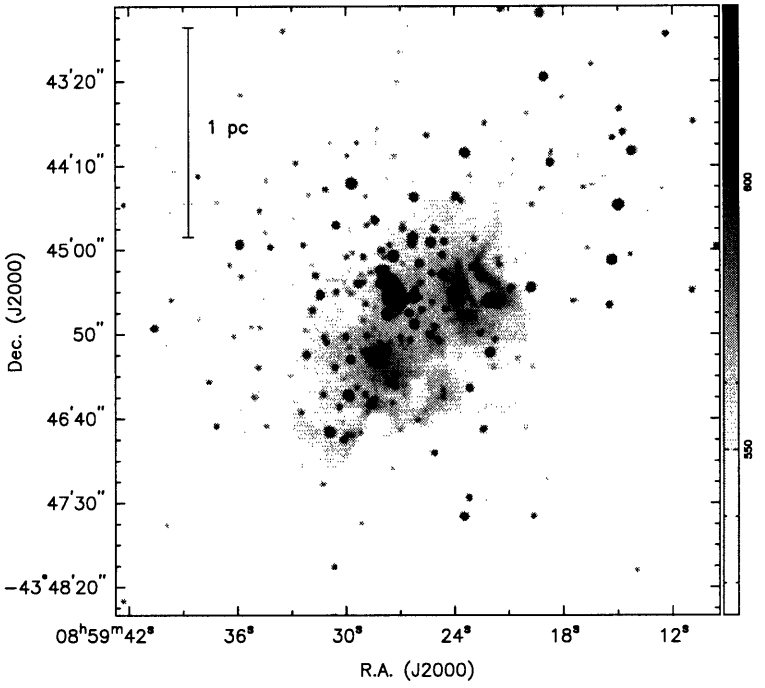

Fig. 5.— A 2MASS near-infrared K-band image of the HII region RCW 36. The stellar cluster can be seen along with diffuse gas emission in the region. The greyscale ranges linearly from 500 to 650 photon counts.

and is located at 08h 57m 38.6s, -43deg 33′47″(1950). The bright source IRAS 08576-4334 detected by the Infrared Astronomical Satellite (IRAS) is also associated with the region.

Far-infrared observations by Verma et al. (1994) concludes the excitation source is either an O8 star or two O9 type stars of Zero Age Main Sequence. They find about 70% of the energy is absorbed by dust and re-radiated in the infrared. They identify two main structures and four faint structures at 58 μm. They also describe the molecular cloud associated with the region to be clumpy.

1.5. RCW 108

RCW 108 is a young compact cluster partially embedded in its parent molecular cloud (Straw et al. 1987). Surrounding RCW 108 is the young OB association Ara OB1. Ara OB1 contains the young galctic cluster NGC 6193 with a cluster age of 5 x 10^6 years (Whiteoak 1963) which is dominated by two early O stars. Figure 15 shows the region in near-infrared.

A bright rim marking the border between the HII region and a dense dark nebula indicated RCW 108 is radiation bounded 15″ to the west of the O star pair. The dark cloud contains a high emission measure knot (Wilson et al. 1970) indicated to be a compact HII region (Frogel and Persson 1974). The comprehensive UBVRI study by Herbst and Havlen (1977) proposed this was a sight of very recent star formation.

Several studies at radio wavelengths have been completed to understand the physical properties of the dark cloud. Goss and Shaver (1970) detected continuum emission at 5 GHz, Caswell and Robinson (1970) detected OH absorption at 1667 MHz, Whiteoak and Gardner (1974) detected H2CO absorption at 4830 MHz, and CO emission at 115 GHz was detected by Whiteoak and Otrupcek (1982). The hydrogen recombination lines H109α and H166α were also measured (Wilson et al. 1970; Cersosimo 1980). In addition to the

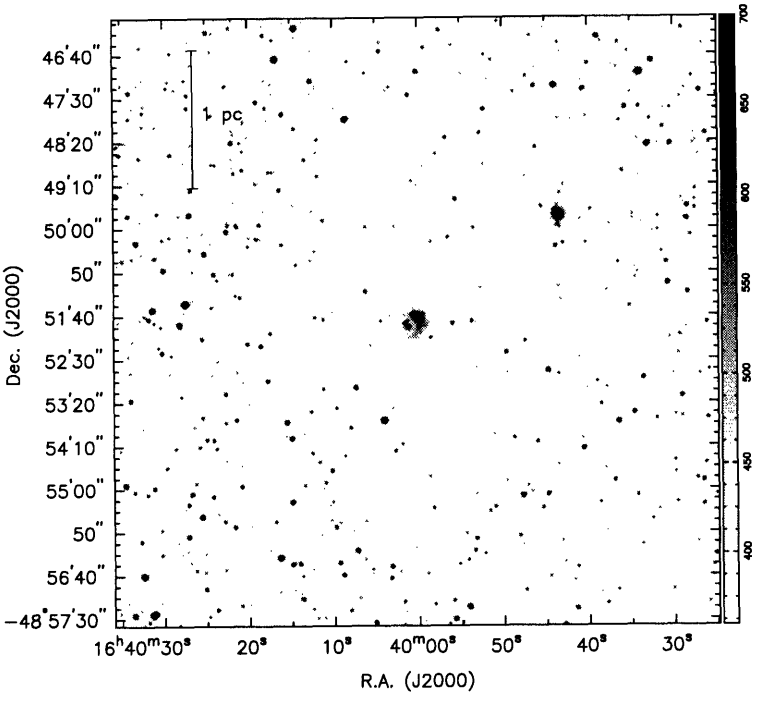

Fig. 6.— A 2MASS near-infrared K-band image of the HII region RCW 108. Generally only a sparse stellar population is visible except for a small cluster of bright stars at the center. The greyscale ranges linearly from 320 to 700 photon counts.

radio studies, IRAS detected intense far-infrared emission (23,000 Jy at 100 μm for a $3'$ x $5'$ beam). The IRAS point source 16362-4845 is associated with RCW 108.

1.6. 1.2 mm Studies

The three HII regions were observed at 1.2 mm to investigate the dust emission in each region. We compare the dust emission to infrared observations as well as radio observations to attempt to understand the interactions between the different components of the regions, specifially relating to star formation.

2. Observations

The 1.2 mm observations were obtained September 2002 and November 2002 with the 37-channel hexagonal bolometer array SIMBA at the Swedish-ESO Submillimeter Telescope (SEST) at La Silla, Chile at an altitude of 2370 meters. SEST is a 15 m diameter radio telescope and operates in the frequency range 70 - 365 GHz and has a pointing accuracy of $3''$ in azimuth and elevation. The HPBW of a single element is about $24''$,and the separation between elements in the sky is $44''$. The pixel sensitivity ranges from 50 to 70 mJy per second.

2.1. Fast Scanning Mode

SIMBA was set to fast scanning mode which means all 37 elements are DC biased requiring scanning at high speeds. The user can input map size and scan speed for each source. For all three sources we used a map size of $20'$ X $20'$ with a scanning speed of $160''$/sec. Five maps were taken for both RCW 38 and RCW 36. Four observations were

made of RCW 108.

2.2. Data Reduction

The data reduction was carried out using the MOPSI (Mapping On-Off Pointing Skydip) software package. Following the steps prescribed in the SIMBA Observers's Handbook (2002), final maps were obtained for RCW 36, RCW 38, and RCW 108. The reduction steps include conversion of the raw data, baseline fitting, despiking, deconvolution, opacity correction, sky noise reduction, calibration and finally map creation.

2.2.1. Conversion of fits files

The raw data files cannot be read by MOPSI, therefore the first step in reduction involves conversion of the fits files through the use of *simbaread* software, written by R. Lemke and M. Albrecht. *Simbaread* accomplishes three tasks. First, it converts the raw files into FITS files which are readable by MOPSI. Second, it determines parameters such as pointing offsets, focus corrections, opacity, tracking accuracy, and map coverage. Third, it creates basic graphical visualizations.

2.2.2. Baseline fitting

Several sources of non-astronomical emission lead to baseline drifts which must be subtracted from the raw data for proper data reduction. The three main sources of this emission are longterm fluctuations due to electronic instability, zero point offsets between the bolometer channels, and spill over emission received by each bolometer channel. These effects are removed or minimized by subracting suitable baselines which are a polynomial

fit to the data of low order (usually less than 3).

2.2.3. Despiking

The data may contain spikes from cosmic rays or electronic discharges which result in artificially high noise levels or modify the actual intensity of the source. Despiking is performed by cutting off signal above a certain noise level depending on the strength of the actual source. The three sources in the study were moderately strong compact sources. Despiking is not necessary for sources which are visible in single maps. All three sources could be clearly seen in single maps therefore despiking was not used in the reduction of the maps to avoid reducing the actual intensity of the sources. Despiking is more important for weak compact sources.

2.2.4. Deconvolution

The pre-amplifier electronics and the bolometer act as an electric oscillator which during fast scanning mode creates a signal distribution containing negative dips. The electronic design and time constants are stored and a matching band-pass filter function is derived. The signals are deconvolved using the filter function to remove the negative dips. The algorithm for deconvolution was created by M. Anciaux, R. Lemke, and M. Nielbock and does not assume a source distribution.

2.2.5. Opacity Correction

Atmospheric extinction modifies the signal intensity. The zenith opacity must be measured during observations to correct for the airmass the signal has passed through. To

obtain the zenith opacity, skydips are performed throughout an observing run to derive the elevation dependent correction factor. The zenith opacity is determined using the relation,

$$S_{em} = S_o exp\left(\frac{-\tau}{sin\ h}\right) \tag{1}$$

where S_{em} is the measured flux, S_o is the unextincted flux, τ is the zenith opacity, h is the elevation, and $sin\ h^{-1}$ is the airmass. The skydip data is fit to the above equation to derive τ, the zenith opacity.

2.2.6. Sky Noise reduction

The greatest noise contribution arises from atmospheric fluctuations. These atmospheric fluctuations occur over a large enough size scale that most of the bolometer channels should experience similar changes in flux. Elimination of this noise increases the signal-to-noise of the source. Residual noise could be left behind if the atmospheric fluctuations are not identical in each channel. The procedure involved determining the 6 best correlated channels and subtracting the median caluculated noise from all the channels.

2.2.7. Calibration

The counts returned by MOPSI must be converted into physical quantities. This is accomplished through the use of a planet map whose intinesities are well known and easy to obtain. The primary calibrator used in this study was the planet Uranus. The planet was observered several times throughout the observing run. The planet data was reduced similar to the target regions, but without despiking and sky noise reduction. The theoretical flux for the position and distance of Uranus at the time of observation was calculated using the

sub-program PLANET in MOPSI. Photometry on the Uranus maps was then performed to derive the conversion factor in mJy/count for the intrument at the time of the observations. The conversion factor for the observations of RCW 38 and RCW 36, which were observered during the same run, was 52 mJy/count. The conversion factor for the observations of RCW 108 was 76.4 mJy/count.

2.2.8. Map Creation

The final step before analysis involves co-adding all the channel maps and transforming the coordinate system to equatorial coordinates. The final maps were the result of co-adding all the observations of each source, transforming the coordinate systems and applying the calibration factors to obtain final images to be analyzed.

3. Results

3.1. RCW 38 Morphology

The 1.2 mm emission in RCW 38 generally follows a ring shape with a long extension to the northeast. The 1.2 mm emission can be seen in Figure 7 with the positions of IRS2 and IRS1 indicated by the white star and triangle respectively. A large cavity lacking emission is found approximately in the center of a ring of emission excluding the extension to the north. The cavity is well centered on the position of IRS2.

The mm emission in the ring surrounding IRS2 is not uniform. Several clumps are seen with the most prominent being a bright peak to the west of IRS2 and offset from IRS1 by approximately 10″. Three other peaks can be detected around IRS2; one directly north, one to the northeast, and one to the south. The bulk of the emission is concentrated within

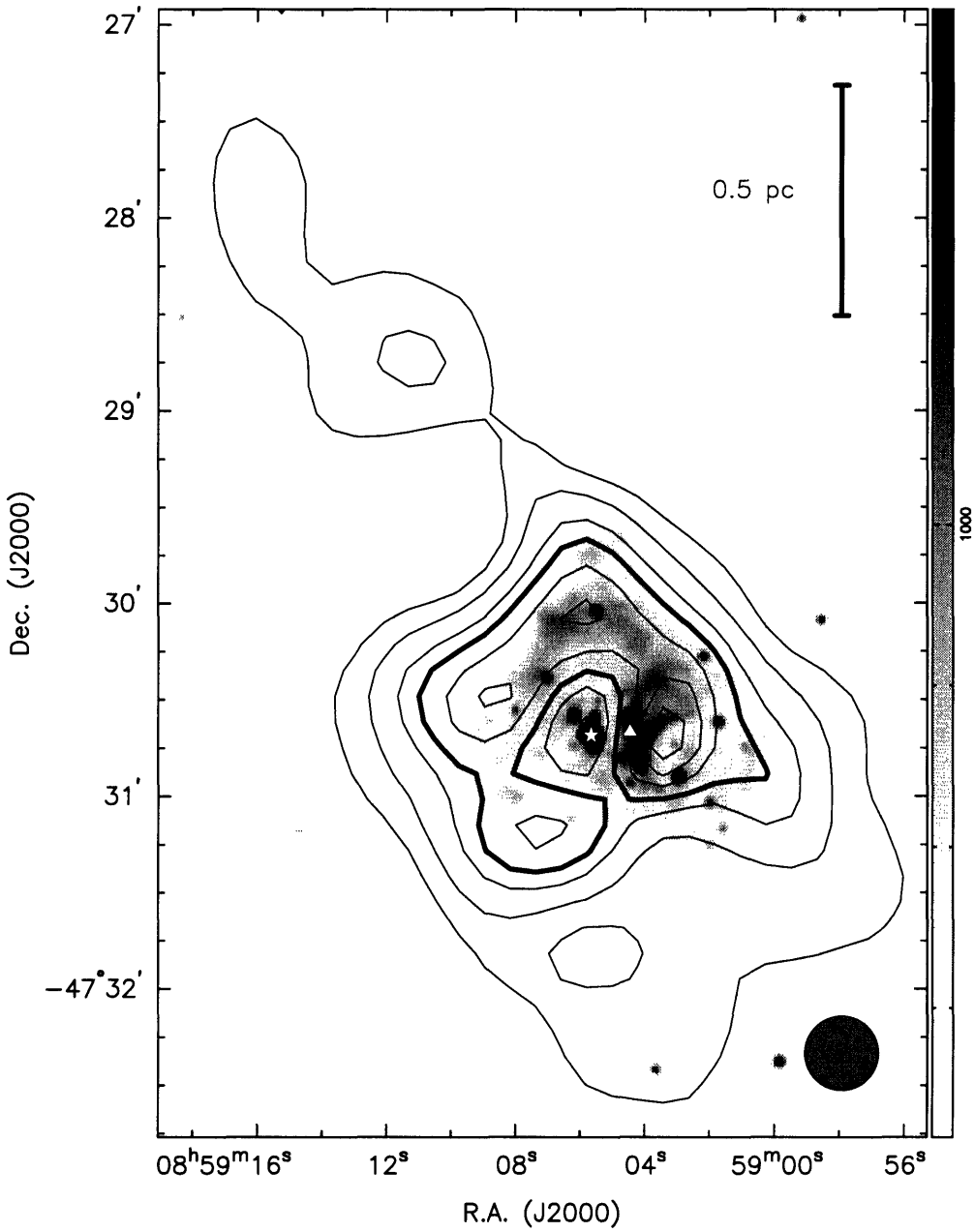

Fig. 7.— 2MASS K-band greyscale of RCW 38 with 1.2 mm contours of 5, 15, 30, 45, 60, 75, and 90 percent of the maximum emission of 5.1 Jy located near the position of IRS1 denoted by the white triangle. The bold contour is the 45% contour level. The white star indicates the position of IRS2. The beamsize of the 1.2 mm observations is shown in the lower right corner. The greyscale ranges linearly from 0 to 2000 photon counts.

a radius of about 1′ making the diameter of the cloud on the order of a parsec.

1.2 mm emission traces dust with a temperature around 20 K. The morphology suggests a region with relatively small dust density in the center and then a ring of dust containing large clumps. The most massive clump is found 20 ″ to the west of the IRS2.

3.1.1. Comparison of 1.2 mm with Near-Infrared Observations

Figure 8 shows a high resolution Very Large Telescope infrared K-band emission observation of RCW 38 with 1.2 mm contours overlaid. The visible star IRS2 can be seen centered within the cavity of the 1.2 mm emission. Diffuse gas can be seen to the northwest of IRS2 with an arc-like ridge to the west, followed by a cavity. The peak emission at 1.2 mm falls within this K-band cavity. The bright ridge roughly coincides with both the position of IRS1 (the peak emission at 10 microns) and the peak emission at 6 cm. The ridge forms an arc and closely borders the edge of the K-band cavity.

The stellar popultion as well as diffuse gas emission are traced by K-band emission. From the morphology, the region appears to have the O star IRS2 centered within a ring of 20 K dust. Diffuse gas is spread throught the region with a ridge of gas followed by a cavity located to the west. This cavity coincides with a clump of 20 K dust.

3.1.2. Comparison of 1.2 mm with 6 cm

The morphologies of the ionized gas traced by 6 cm emission and the cold dust traced by 1.2 mm emission closely parallel each other. Figure 9 shows 6 cm contours over 1.2 mm greyscale emission. Both observations reveal emission in a ring-like structure with a cavity roughly centered on IRS2. The 6 cm cavity is offset to the northwest of the 1.2 mm cavity

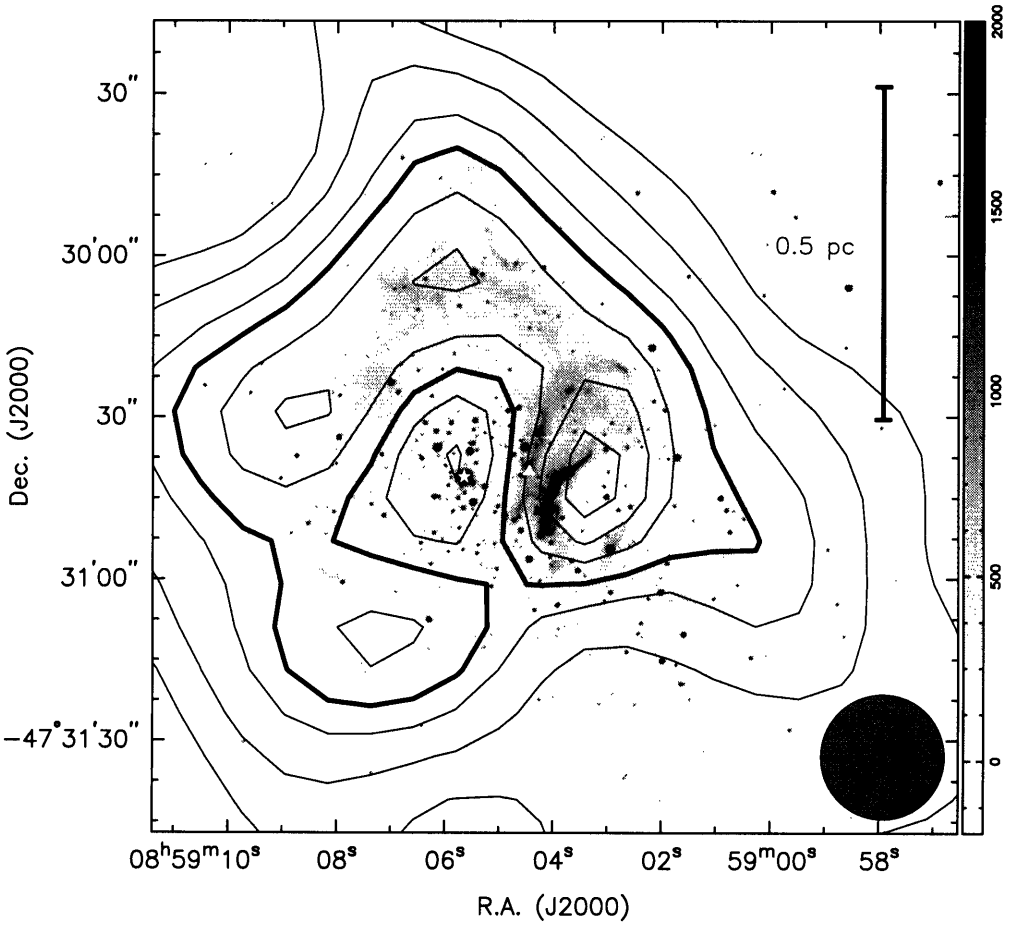

Fig. 8.— A K-band greyscale VLT image of RCW 38 with 1.2 mm contours of 15, 30, 45, 60, 75, and 90 percent of the maximum emission of 5.1 Jy. The bold contour represtnts the 45% contour. The beamsize of the 1.2 mm observations is shown in the bottom right corner. The white star indicates the position of IRS2 and the white triangle indicates IRS1. the greyscale rangels linearly from -200 to 2000 photon counts.

by approximately 10″. Four bright clumps in the ring can be detected with the brightest being on the west edge near IRS1. The peak 6 cm emission is offset from both the peak at 1.2 mm and at 10 microns (IRS1). The peak lies between the two other peaks with the bright 1.2 mm clump offset by 5 arcseconds to the west, however, the 6 cm peak is coincident with the arc-like ridge in the K-band.

These morphologies suggest the central region is devoid of 20 K dust as well as ionized hydrogen. A ring of both ionized hydrogen and dust surround IRS2 with the radio ring slightly interior of the 1.2 mm ring. The offset of the two bright clumps indicates the dust surrounds the ionized hydrogen.

3.1.3. Comparison of 1.2 mm with 8, 10, and 20 micron emission

The Midcourse Space Experiment (MSX) obtained observations of RCW 38, RCW 36 and RCW 108 at 8, 12, 14 and 21 microns. The 8 micron emission contains PAH bands while the 12 and 14 micron emission mainly traces thermal emission or warm dust. 21 micron emission traces thermal emission as well as hydrogen gas. The MSX observations for the three star forming regions are compared to the 1.2 mm emission to understand morphology and interactions of gas and dust in the regions. MSX 8 micron observations are four times more sensitive than previous IRAS 12 micron observations.

Emission at 1.2 mm appears to surround emission at 10 and 20 microns. Figure 10 compares 8μm and 21μm emission with 1.2 mm emission. MSX E-band emission at 21 microns also exhibits a circular structure similar to that of the 1.2 mm emission. It also exhibits a peak to the west near IRS1. This peak is not coincident with the 1.2 mm, 6 cm peak, or the ridge at 1.2 microns. IRS1 identified by Smith et. al. (1999) as the peak in the 10 micron emission lies interior to all the other peaks. It is offset by a few arcseconds

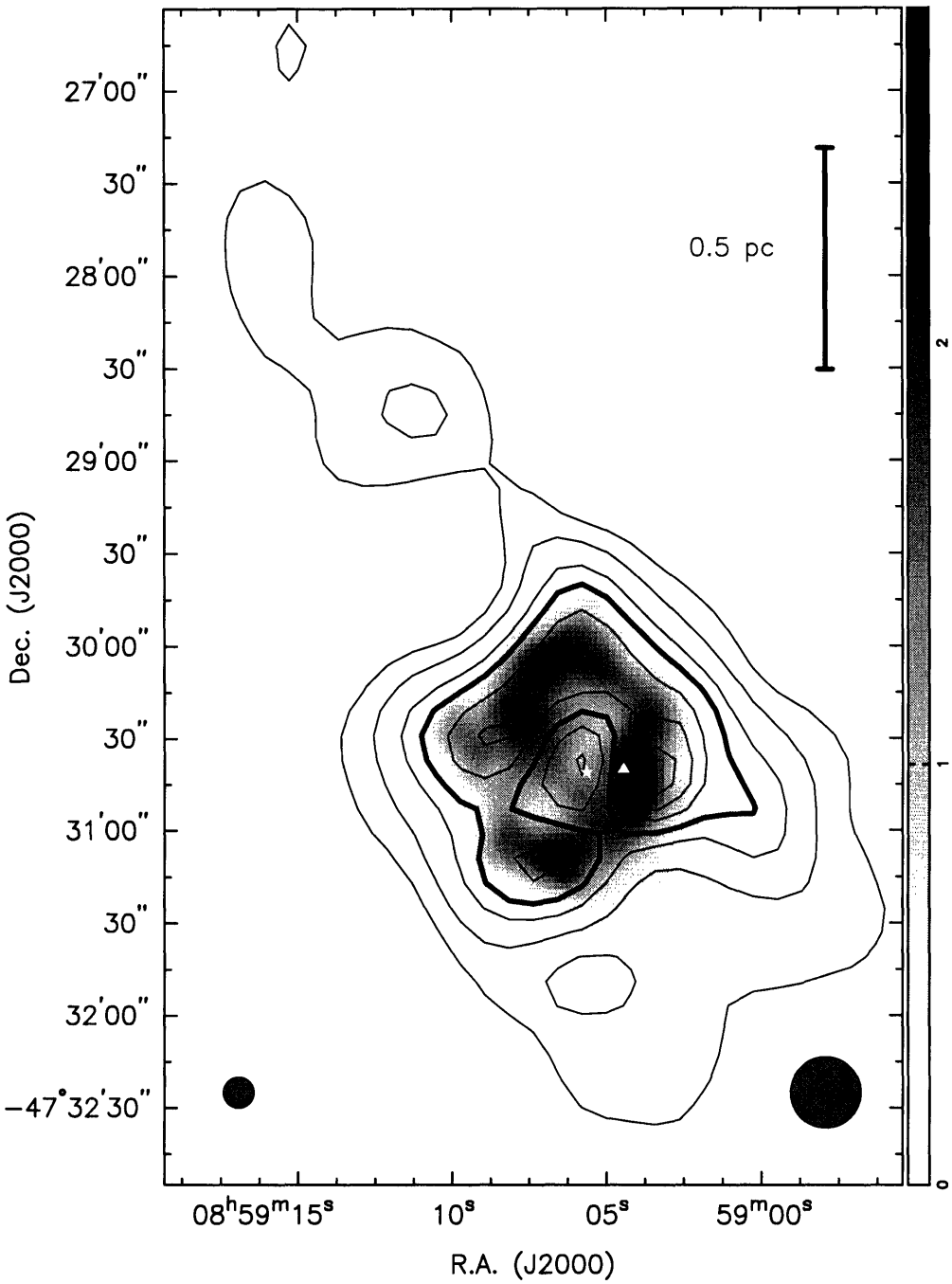

Fig. 9.— RCW 38 with 1.2 mm contours of 5, 15, 30, 45, 60 ,75, and 90 percent of the maximum emission over a 6 cm greyscale image. The bold contour line represents the 45% contour level. The greyscale image ranges from 0 to 2.5 Jy/beam. The white star indicates the position of IRS2 and the white triangle indicates IRS1. The beamsize of the 6 cm observations is shown in the lower left, and the 1.2 mm beamsize is shown in the lower right.

to the east. MSX 8 micron emission peaks right on the position of IRS1 and only extends slightly to the east. It generally is concentrated around IRS1. In general the 10-20 micron emission lies interior to the 1.2 mm and 6 cm emissions.

The 10 micron emission traces relatively warm dust compared to the dust traced at 1.2 mm. Smith et al. (1999) calculate a dust temperature at 10 microns between 140-180 K in the region. 21 micron emission contains contamination of hydrogen gas as well as dust. Assuming the offsets are real and not mearly resolution effects or pointing errors, the morphology of the emissions suggest ~170 K dust on the interior of the 6 cm peak, and 1.2 micron gas ridge, and then colder dust of temperature 20 K outside the gas ridge.

3.1.4. Dust Emission and Mass

The dust mass and density distribution in the molecular cloud were calculated using the optically thin 1.2 mm emission. Dust masses were calculated using the relation,

$$M_{dust} = \frac{S_\nu D^2}{\kappa_{\nu,d} B_\nu(T_d)} \tag{2}$$

where S_ν is the observed dust emission, $\kappa_{\nu,d}$ is the dust opacity per unit mass column density and $B_\nu(T_d)$ is the Planck function for a dust temperature T_d (Chini et al. 2003). The masses were calculated assuming a dust temperature of 20 K and using a dust opacity of 0.37 $cm^2 g^{-1}$ which is a value consistent for the diffuse ISM but may increase by up to a factor of 10 in dense regions or protostellar environments (Ossenkopf & Henning, 1994).

The distribution of mass throughout the HII region was investigated by calculating the mass in the entire region, the mass in the dust ring, and the mass in the large clump located near IRS1. The total mass was calculated from the flux within the outer contour at 30% of maximum emission. The ring mass was calculated as the whole emission with the

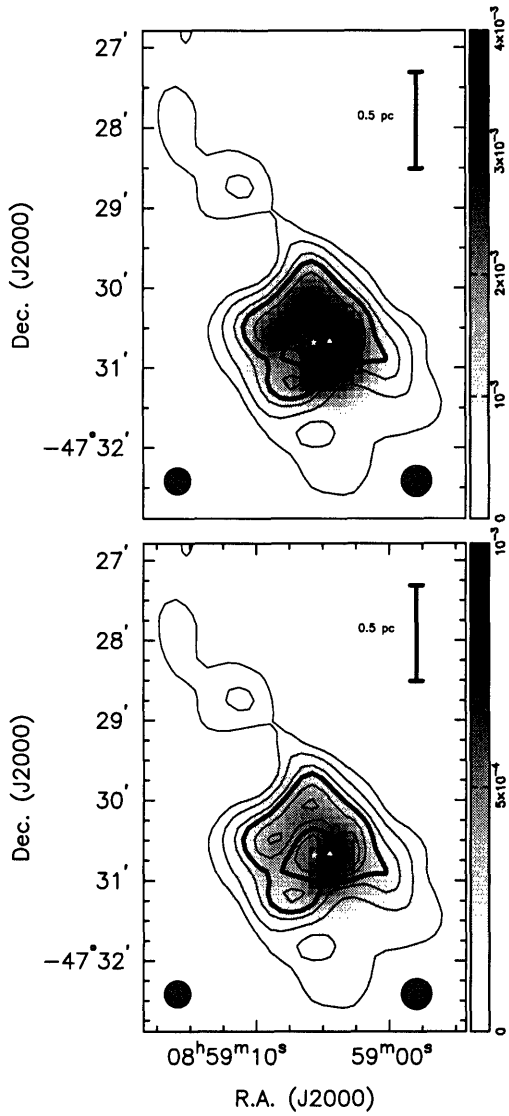

Fig. 10.— The upper figure is RCW 38 with 1.2 mm contours of 5, 15, 30, 45, 60, 75, and 90 percent of the maximum emission over a 21μm greyscale MSX image.The greyscale ranges from 0 to 0.004 W m^{-2} sr^{-1}. The lower image is RCW 38 with 1.2 mm contours of 5, 15, 30, 45, 60 ,75, and 90 percent of the maximum emission over a 8μm greyscale MSX image. The greyscale ranges from 0 to 0.001 W m^{-2} sr^{-1}. The bold contours represents the 45% contour level. The white star indicates the position of IRS2 and the white triangle indicates IRS1. The beamsize of the 1.2 mm observations is shown in the lower right corner and the beamsize of the MSX images are to the lower left.

central cavity subtracted. The cavity was defined as the region within the smaller contour of 30% of maximum emission. The bright clump near IRS1 contain the peak emission and was defined as the 65% of maximum emission contour. Figure 11 shows the regions and the results are given in Table 2.

The total flux from the region is close to 350 Jy which we calculate to indicate a total mass of 276 solar masses. The morphology of the region indicates that the dust is actually concentrated within a ring surrounding an empty cavity. The flux from the cavity was only 6.2 Jy indicating only about 6 solar masses of dust reside within about a 10″ radius of IRS2. Subtracting the cavity from the total mass yields the mass in the ring of 271 solar masses. The ring then contains 98% of the total mass in the region, and the cavity only about 2%. The bright clump near IRS1 contains close to 50 solar masses of dust and contains 18% of the total mass in the region.

3.2. RCW 36 Morphology

RCW 36 can be seen at 1.2 mm as a ridge running southeast to northwest seen in Figure 12. It is about 1.5 parsecs in length and is located to the southwest of the majority of the visible clustered stars. The emission is not uniform and two individual clumps can be resolved. The brightest clump which contains the peak emission is located at the northwest edge of the ridge. The peak emission in this clump is 1590 mJy. The second peak is in the central region of the ridge. Small faint individual clumps can be seen around the southeast edge of the ridge and a faint line of emission can be seen to the north.

The dust traced at 1.2 mm appears in a linear ridge without apparent interaction with the nearby stars. Smaller clumps and ridges of dust are spread throughout the region though the main collection of dust is within the ridge.

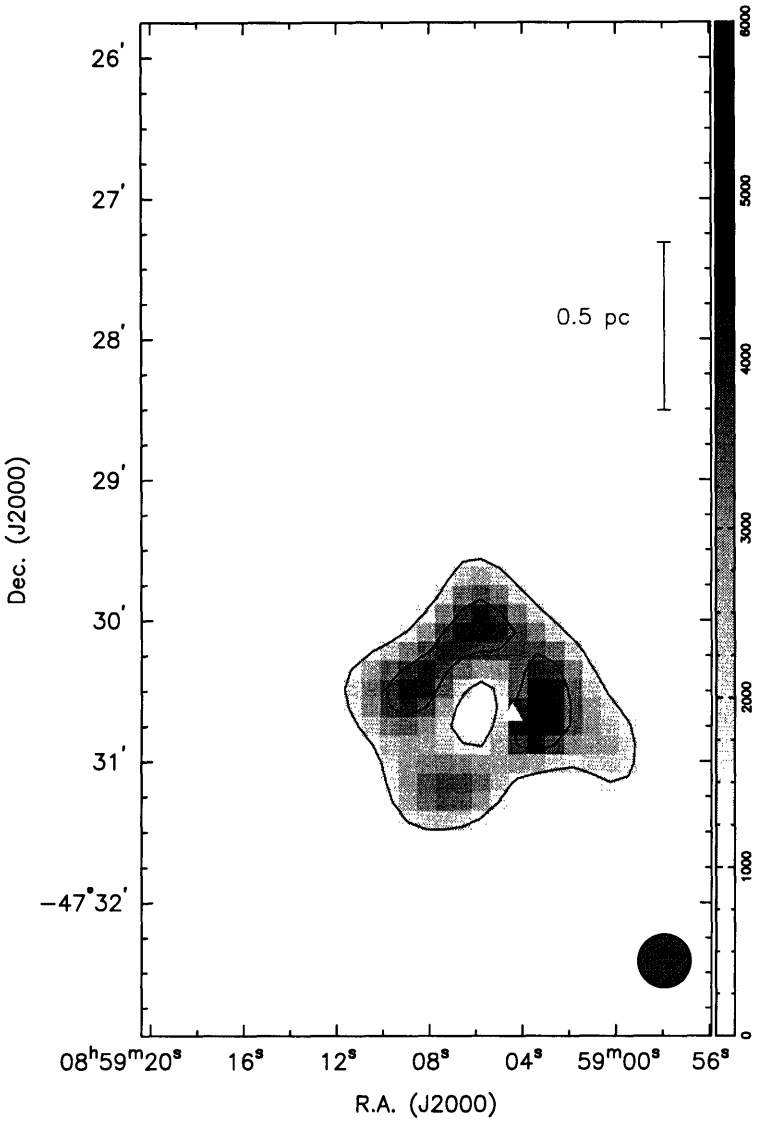

Fig. 11.— 1.2 mm greyscale image of RCW 38 with countours of 30% and 65% of maximum emission. The greyscale ranges from 0 to 6000 mJy. The entire region is defined to be contained within the outer 30% contour. The cavity is defined as the area within the smaller 30% contour containing IRS2. The ring is the whole area minus the cavity. The clump near IRS1 is defined as the 65% contour touching IRS1. The white star indicates the position of IRS2 and the white triangle indicates IRS1. The beamsize of the 1.2 mm observations is shown in the lower right corner.

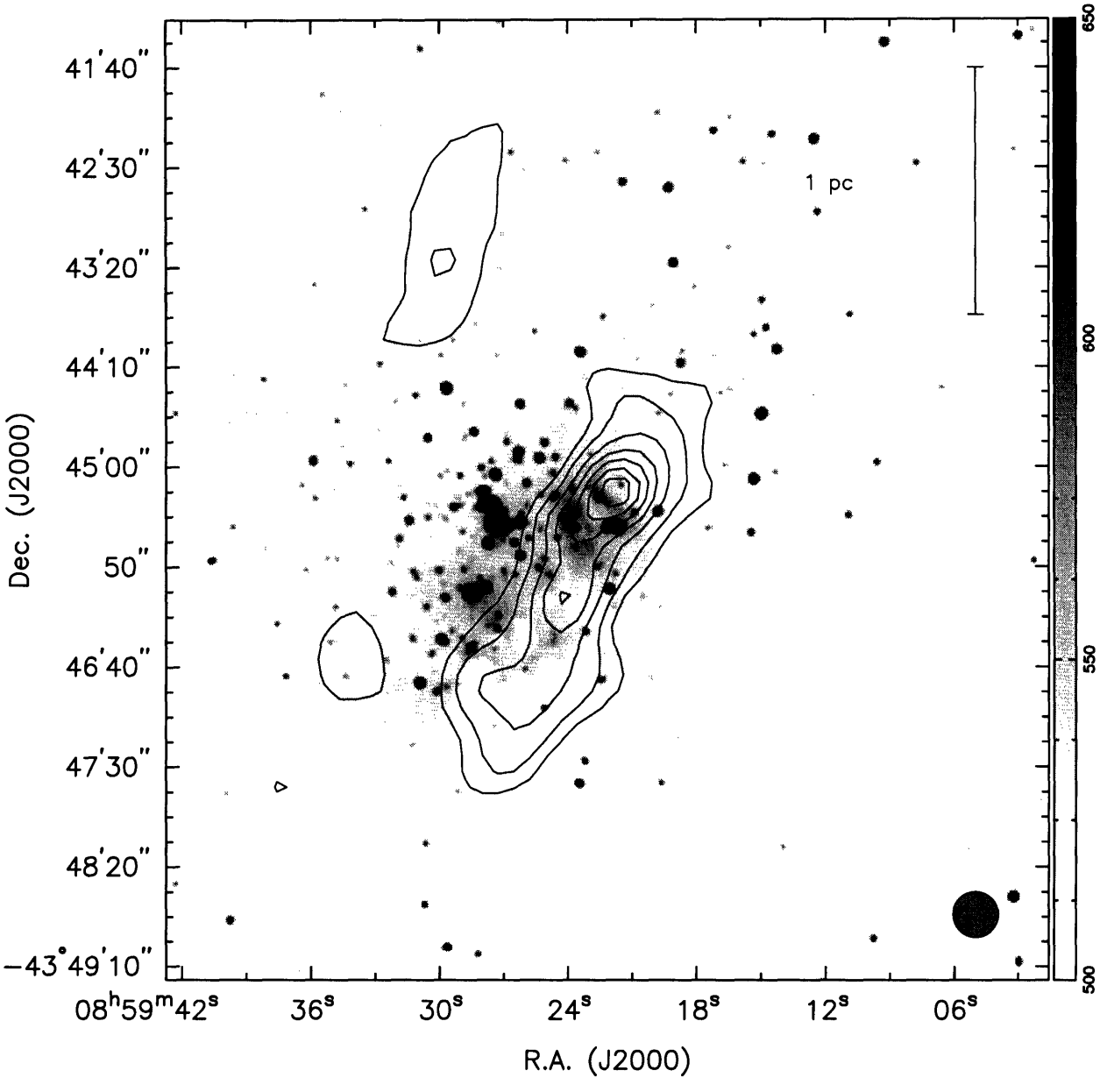

Fig. 12.— RCW 36 at 1.2 mm with contours of 5, 15, 30, 45, 60 ,75, and 90 percent of the maximum emission of 1.59 Jy over a gray scale 2MASS k-band image. The 1.2 mm beamsize is located in the lower right corner. The greyscale ranges from 550 to 650 photon counts.

3.2.1. Comparison of 1.2 mm with Infrared K-Band emission

Peak emission at 1.2 mm appears to be located to the south of the densest area of stars seen by 2MASS, Figure 12. It possibly overlaps with the bottom of a cavity of the diffuse emission seen by 2MASS. The bright stars are well to the north and east of the 1.2 mm emission and do not obviously appear to be interacting with the dust. The dense stellar population of stars is not coincident with the dust emission, and the dust tends to reside in areas devoid of visible stars and diffuse gas except near the peak at 1.2 mm. A small clustering of stars can be seen near the 1.2 mm peak as well as some diffuse gas.

3.2.2. Comparison of 1.2 mm with 8 and 21 micron emission

The peak emission at 10-20 microns is roughly coincident with the O star in the cluster. Figure 13 compares MSX E-band morphology with 1.2 mm morphology. The 1.2 mm emission runs along the southwest edge of the micron emission with the 10-20 micron emission extending to the notheast. The dust traced by the 1.2 mm emission is more tightly confined than the dust traced by the 10-20 micron emission.

3.2.3. Dust Emission and Mass

The dust mass in RCW 36 was calculated with the same procedure as was used for RCW 38. Similar to RCW 38, 1.2 mm emission in RCW 36 is clumpy and non-uniform so the mass in specific clumps as well as the total mass was calculated. The total flux within the countour of 30% of the maximum emission was taken as the total extent of the main cloud of dust. The contours which represent 55% of the maximum emission were chosen to depict the two bright clumps within the dust cloud. The primary peak as well as a secondary peak to the south were defined by the countour lines as seen in Figure 14. The

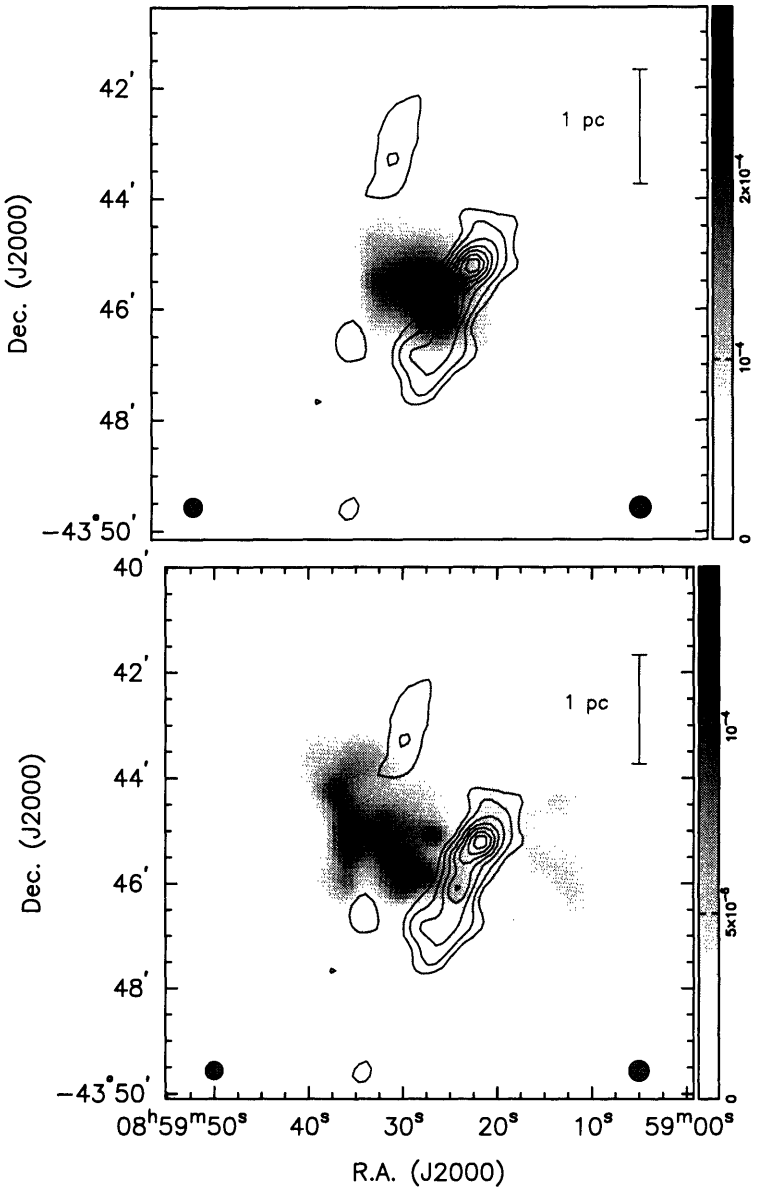

Fig. 13.— The upper figure is RCW 38 with 1.2 mm contours of 5, 15, 30, 45, 60, 75, and 90 percent of the maximum emission over a 21μm greyscale MSX image.The greyscale ranges from 0 to 0.0003 W m^{-2} sr^{-1}. The lower image is RCW 38 with 1.2 mm contours of 5, 15, 30, 45, 60 ,75, and 90 percent of the maximum emission over a 8μm greyscale MSX image. The greyscale ranges from 0 to 0.0001 W m^{-2} sr^{-1}. The beamsize of the 1.2 mm observations is shown in the lower right corner and the beamsize for the MSX images are to the lower left.

results are reported in Table 2.

The total dust cloud consists of close to 50 solar masses of dust. The bright primary peak contains 34 solar masses of dust which is 70.5% of the total mass in the cloud. The smaller peak only contains 6.1 solar masses but still represents close to 13% of the total mass in the cloud. It is clear that the majority of the material in the region is clustered in the northern edge of the 1.2 mm dust ridge.

3.3. RCW 108

3.3.1. Morphology

The morphology of the 1.2 mm emission is concentrated in a linear ridge running northeast to southwest with an extension to the east at the southern edge. Figure 15 shows the extent of the 1.2 mm emission. The emission extends approximately 0.6 parsecs from north to south. Unlike RCW 38 and RCW 36, the dust emission from RCW 108 is concentrated around one region without any secondary clumps and only the slight extension in the south. The peak emission is about 5 Jy at the center of the ridge.

3.3.2. Comparison of 1.2 mm with 1.2 microns

Figure 15 shows a 2MASS K-band image of RCW 108 with 1.2 mm contours. The stellar population surrounding the 1.2 mm emission is extemely sparse or obscured by dust, however, several bright sources can be seen clustered near the peak emission at 1.2 mm. The dust emission coincides with the central stellar population in the K-band image. The extension to the south is not coincident with any visible source.

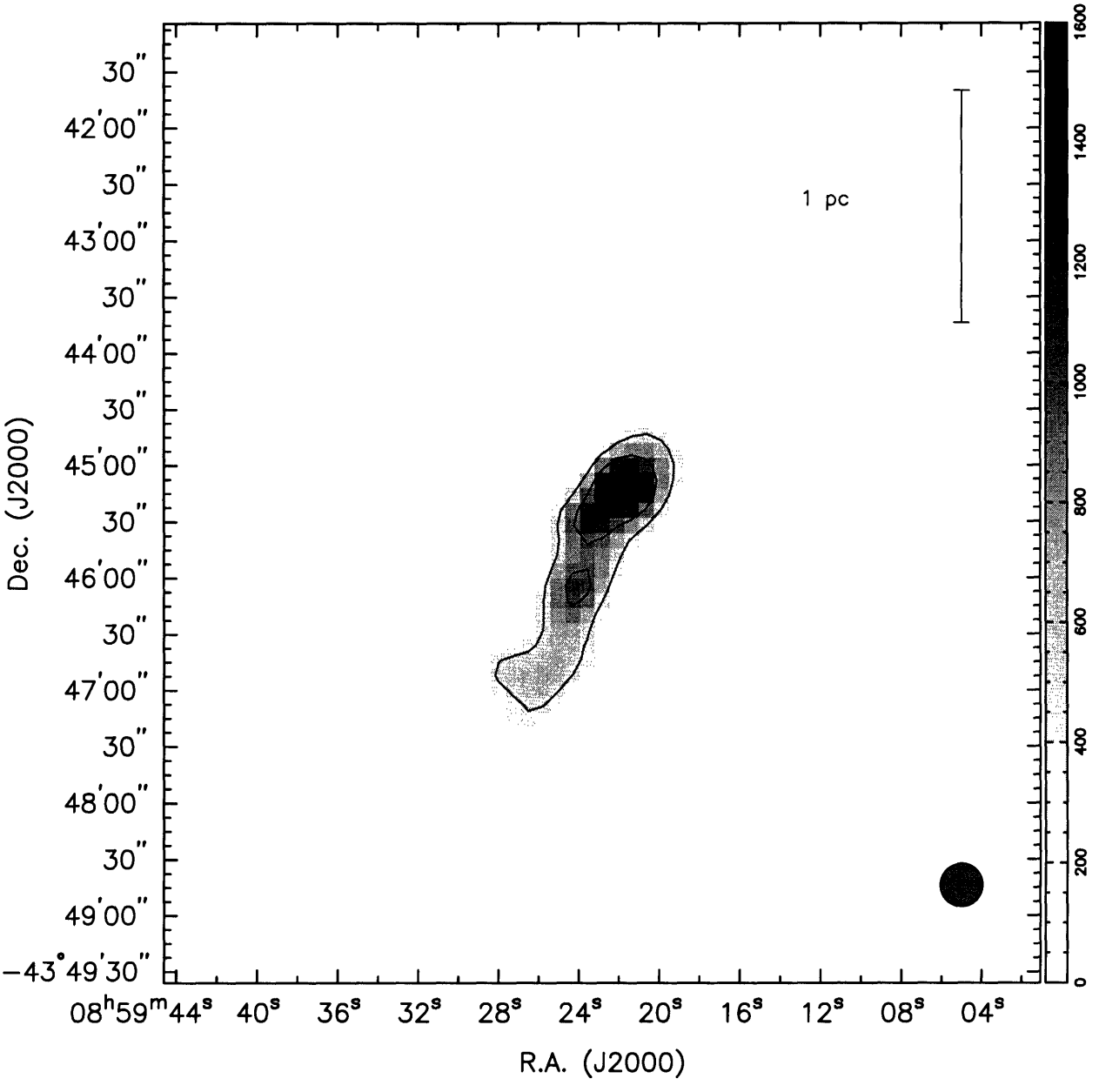

Fig. 14.— 1.2 mm greyscale image of RCW 36 with countours of 30% and 55% of maximum emission. The entire region is defined to be contained within the outer 30% contour. The northern clump is the area within the larger 55% contour level and the smaller contour defines the secondary peak.

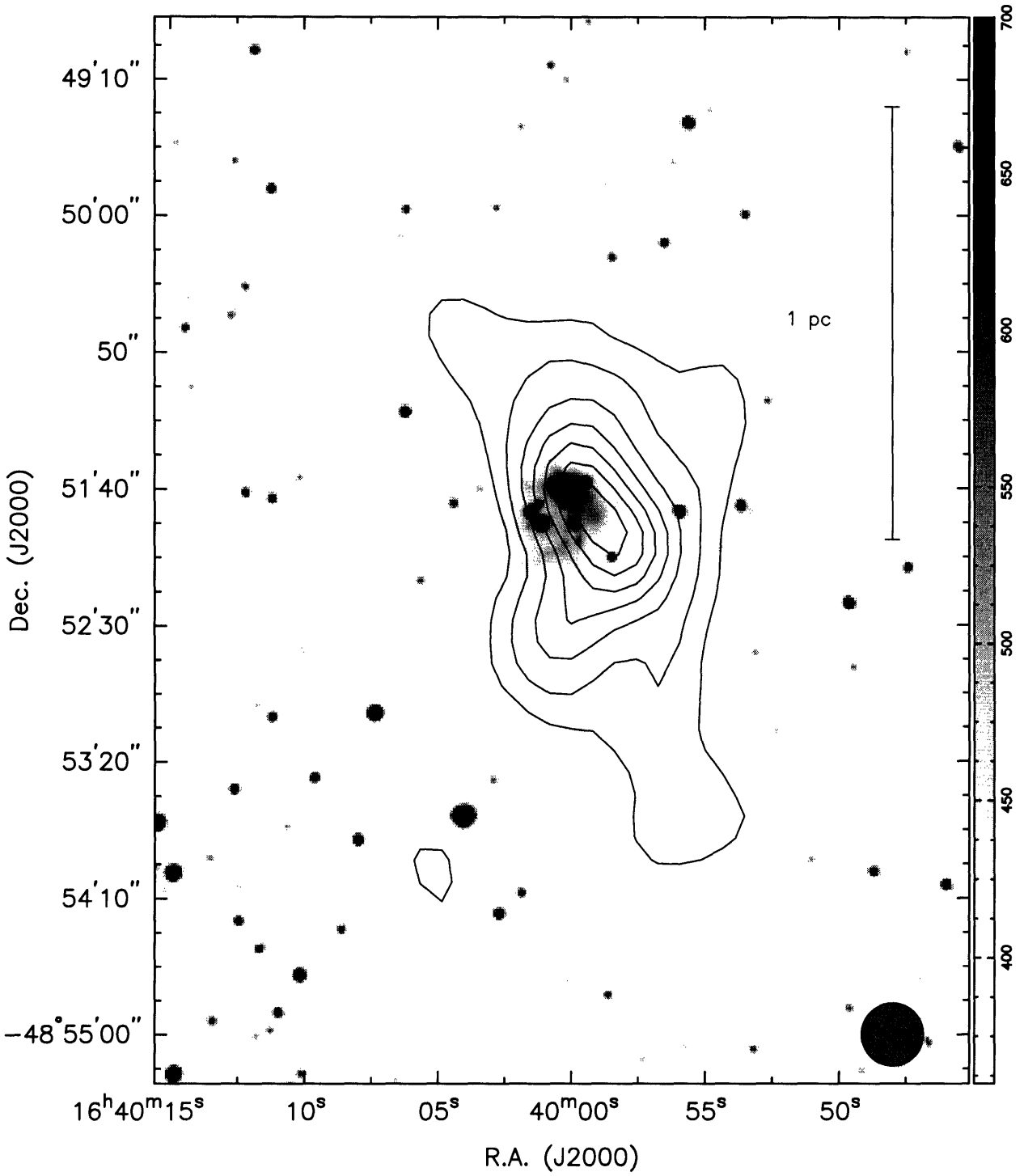

Fig. 15.— RCW 108 with 1.2 mm contours of 5, 15, 30, 45, 60 ,75, and 90 percent of the maximum emission of 5.26 Jy over a 2MASS k-band greyscale image. The greyscale ranges linearly from 320 to 700 photon counts.

3.3.3. Comparison of 1.2 mm with 8 and 21 micron emission

Morphology of 21 micron emission roughly follows the general morphology of the 1.2 mm emission as seen in Figure 16. The 21 micron emission is concentrated in one fairly circular clump coincident with the clump at 1.2 mm. The extent of the 21 micron emission is less than the 1.2 mm. The bulk of the emission is wthin the 1.2 mm ridge with the micron emission extending slightly more toward the east than the 1.2 mm emission. The morphology of RCW 108 at 1.2 microns, 10-20 microns and 1.2 mm show the bulk of the emission concentrated in one location near a cluster of stars.

3.3.4. Dust Emission and Mass

The vast majority of the emission from RCW 108 is concentrated in one clump with. Seperate clumps or structures can not be resolved in RCW 108. The total mass of the region was determine from the flux within a countour of 30% of the maximum flux in the region. The total mass was determined to be 147.8 $\pm$ 12.2 solar masses. The flux from the region was 189.6 $\pm$ 0.4 Jy.

4. Discussion

4.1. Star Formation in RCW 38

The O star IRS2 appears to be determining the general shape and extent of the dust and gas morphology in RCW 38. Both 6 cm emission and 1.2 mm emission exhibit ring structures roughly centered on IRS2. These structures could be the result of massive O-star winds originating from IRS2. The winds could be excavating gas and dust from it's near vicinity creating a shell of material enclosing IRS2.

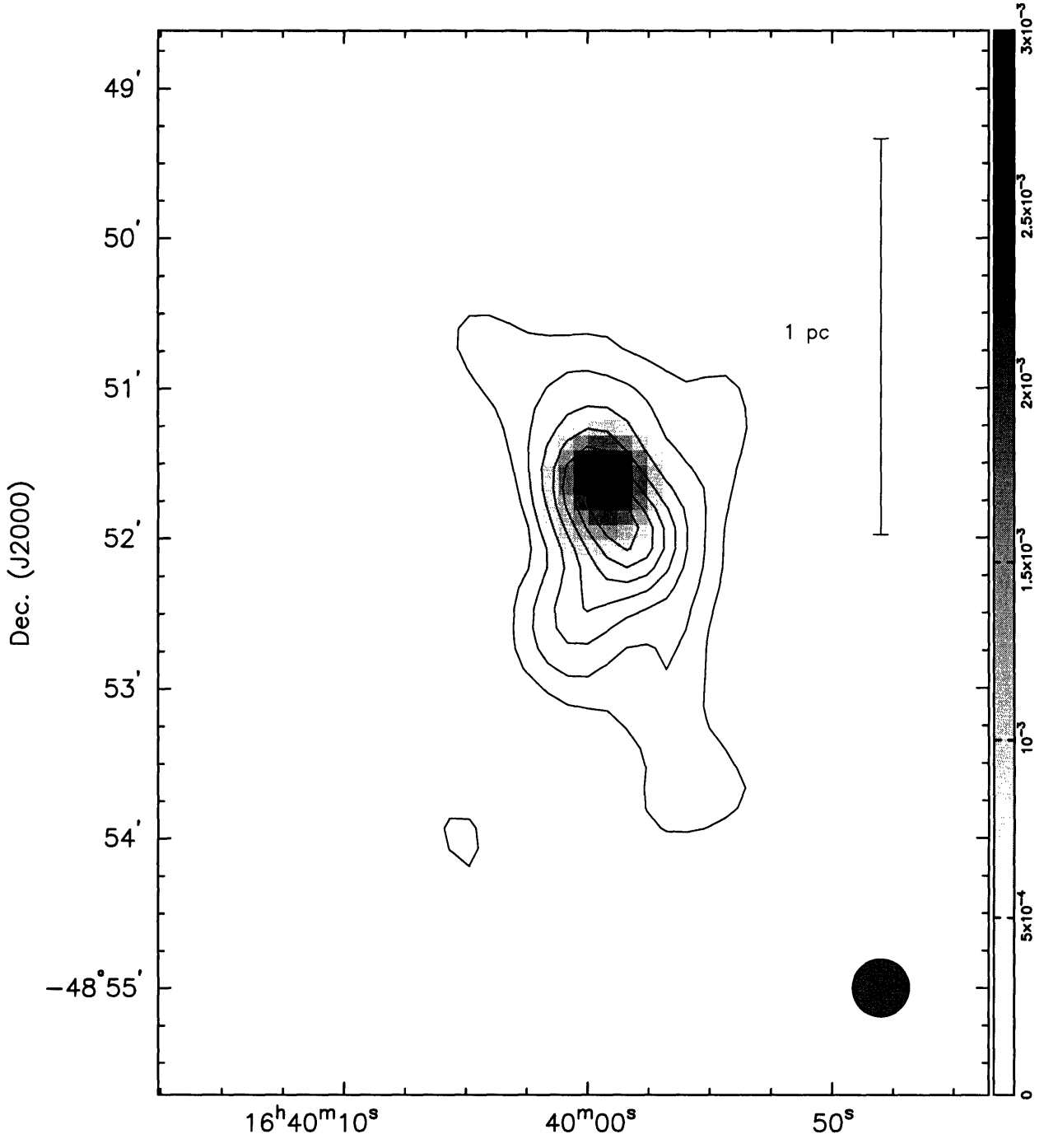

Fig. 16.— RCW 108 with 21μm contours of 15, 30, 45, 60 ,75, and 90 percent of the maximum emission with a 1.2 mm greyscale image.

The second important feature in RCW 38 is the region located near the position of IRS1. Strong emission is detected at 6 cm, 1.2 mm, 10 microns as well as 1.2 microns suggesting this could be a sight of current or future star formation. It should be noted that the peak emission at each wavelength do not perfectly coincide. The K-band ridge coincides with a similar ridge at 6 cm but the peaks seen at 10 microns and 1.2 mm are offset from these locations. Figure 17 compares the 6cm emission, 1.2 mm emission, and the K-band emission.

The dust traced by 1.2 mm emission is located to the west of the 6 cm ridge and fills in a cavity in the K-band emission. The K-band ridge borders the 1.2 mm dust emission. The micron emission which can be represented by the position of IRS1 (the peak at 10 microns) is offset to the east of the 6 cm peak. The dust emissions traced by 10 micron emission and 1.2 mm emission appear to be surrounding a region filled with hot hydrogen gas. We see warm ($\sim$170 K) on the inner edge of the ring, a build up of hydrogen gas in the interior and a clump of colder ($\sim$20 K) dust toward the outer edge. The shape of the ridge in the K-band emission suggests a bow shock, possibly formed by the expanding shell from IRS2 encountering a clump of dust and being deflected around this dense region to form its current shape.

Previous studies at 6 cm revealed the geometric centroid of the region was offset from the position of IRS2 by 5″. The centroid is shifted to the east relative to IRS2. Assuming a freely expanding shell, the geometric center of the region should remain at the position of IRS2. If in fact, the shell is not expanding freely but has encountered a dust clump which inhibits its expansion to the west while the rest of the ring freely expands, the geometric centroid would be offset to the east. The large clump we detect at 1.2 mm could possibly be prohibiting expansion to the west and would account for the offset to the east of the 6 cm continuum emission.

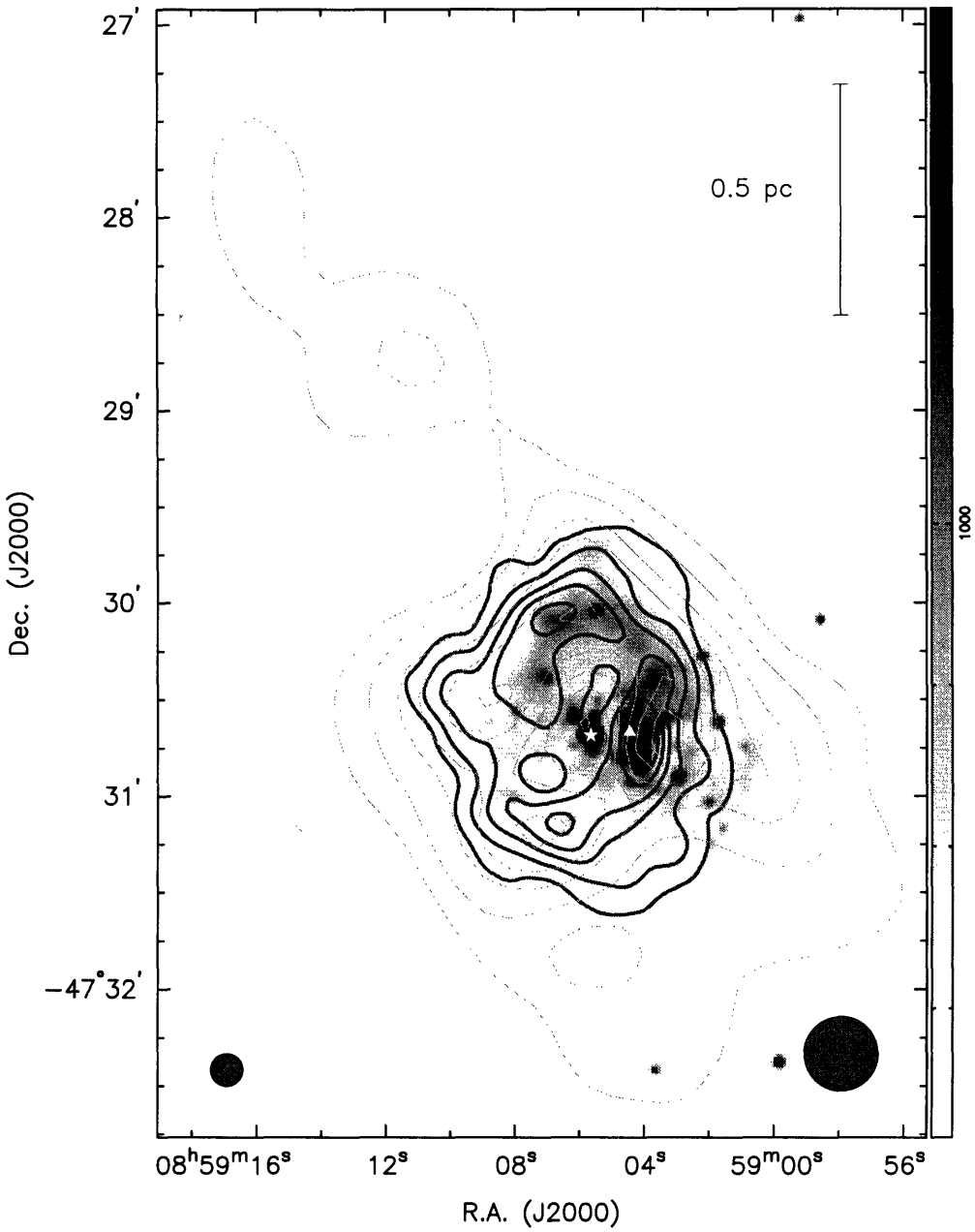

Fig. 17.— RCW 38 K-band greyscale with 1.2 mm contours of 5, 15, 30, 45, 60 ,75, and 90 percent of the maximum emission of 5.26 Jy and 6 cm contours of 15, 30, 45, 60 ,75 and 90 percent of the maximum emission. The bold contours are the 6 cm contours. The beamsize of the 6 cm observations is shown in the lower left and the 1.2 mm beam size to the lower right.

4.2. Star Formation in RCW 36

The HII region RCW 36 has a cluster of stars which for the most part do not coincide with the dust traced at 1.2 mm. A few stars from the K-band image can be seen at the peak of the dust emission. It is possible that previous star formation occured to the north of the dust ridge resulting in the population of stars seen in the K-band and the next area of star formation could possibly be occuring within the dense clump of dust coincident with some gas emission detected in the K-Band and at 21 microns. A stellar cluster was previously formed and there is indications that further star formation may be occuring.

4.3. Star Formation in RCW 108

RCW 108 appears to be the youngest and least evolved of the three HII regions. There is a small stellar population, mostly concentrated at the center of the dust emission. It appears RCW 108 is currently undergoing star formation as we detect some embedded sources within the dust emission we trace at 1.2 mm as well as 10-20 microns.

5. Summary

1.2 mm observations of the HII regions RCW 38, RCW 36, and RCW 108 combined with previous infrared observations and radio observations reveal possible mechanisms for the evolution of the regions. We find RCW 108 to be a relatively young cluster most likely currently undergoing star formation. RCW 36 appear to be slightly more evolved with a more pronounced stellar population similar to RCW 38 which shows a large stellar cluster as well as potential for further star formation.

Table 1. SEST Observing Parameters for RCW 38, RCW 36, and RCW 108

Parameter	RCW 38	RCW 36	RCW 108
Observing Dates	Nov. 13-15, 2002	Nov. 13-15, 2002	Sept. 27-28, 2002
Map Size	$20' \times 20'$	$20' \times 20'$	$20' \times 20'$
Scanning Speed	$160''$/s	$160''$/s	$160''$/s
Total Integration Time (hr)	2.5	2.5	2.0
Total no. of maps	5	5	4
Calib. factor mJy/cnt	52	52	76.4
Beam Size (FWHM)	$24''$	$24''$	$24''$
Distance (kpc)	1.7	1.7	1.3
Size conversion	$1' \sim 0.4845$ pc	$1' \sim 0.4845$ pc	$1' \sim 0.3780$ pc

Table 2. Flux and Dust Mass in RCW 38, RCW 36, and RCW 108

Source	S Jy	Mass M_{sol}	Percent of total
RCW 38			
Ring	342.2± 0.6	271.1± 16.6	98.2
Cavity	6.2 ± 0.1	5.8± 2.4	1.8
IRS1 clump	52.4 ± 0.2	48.9± 7.0	18.0
Total	348.4 ± 0.6	276.3 ± 16.6	100.0
RCW 36			
Primary Peak	23.7 ± 0.2	33.8 ± 5.2	70.5
Secondary Peak	3.7 ± 0.1	6.1 ± 2.5	12.8
Total	36.7 ± 0.2	48.1 ± 6.9	100.0
RCW 108			
Total	189.6 ± 0.4	147.8 ± 12.2	100.0

REFERENCES

Brand. J., van der Bij, M.D.P., de Vries, C.P., Leene, A., Habing, H.J., Isreal, F.P., de Graauw, T., van de Stadt, H., Wouterloot, J.G.A., 1984, *Astronomy and Astrophysics*, 139, 181-195

Braz, M.A., Epchtein, N., 1982, *Astron. Astrophys.*, 111, 91-96

Braz, M.A., Scalise, Jr., 1982, *Astron. Astrophys.*, 107, 272-275

Brooks, K.J., Storey, J.W.V., Whiteoak, J.B., 2001,*MNRAS*, 327, 46-54

Caswell, J.L., Haynes, R.F., 1987, *Astron. Astrophys.*, 171, 261-276

Caswell, J.L., Robinson, B.J., 1974, *Australian J. Phys.*, 27,597

Cersosimo, J.C., 1982, *Ap. Letters*, 22, 157

Chini, R., Kampgen, K., Reipurth, B., Albrecht, M., Kreysa, E., Lemke, R., Nielbock, M., Reicherts, L.A., Sievers, A., Zylka, R., 2003, *Astron. Astrophys.*, 409, 235-244

Cheung, L.H., Frogel, J.A., Gezari, D.Y., Hauser, M.G., *The Astrophysical Journal*, 240, 74-83

De Pree, C.G., Nysewander, M.C., Goss, W.M., 1999, The Astronomical Journal, 117:2902-2918

Frogel, J.A. & Persson, S.E., 1974,*ApJ*, 192, 351

Goss, W.M., Shaver, P.A., 1970, *Australian J. Phys.*, 14, 1

Herbst, W., Havlen, R.J., 1977, *Astr. Ap. Suppl.*, 3-, 279

Molinari, S., Brand, J., Cesaroni, R., Palla, F., Palumbo, G.G.C., 1998, *Astron. Astrophys.* 336, 339-351

Murden, Paul, 2001, *Encyclopedia of Astronomy and Astrophysics*, Nature Publishing Group, 4, 1-5

Rodgers, A.W., Campbell & Whiteoak 1960, *MNRAS*, 121, 123

Roelfsema, P.R., Goss, W.M., 1992, A&A, 4, 161

Shu, F.H, Adams, F.C., Lizano, S., 1987, *Ann. Rev. Astron. Astrophys.*, 25: 23-81

Smith, C.H., Bourke, T.L., Wright, C.M., Spoon, H.W.W., Aitken, D.K., Robinson, G.; Storey, J.W.V., Fujiyoshi, T., Roche, P.F., Lehmann, T., 1999, *MNRAS*, 303, 367

Straw, S., Hyland, A.R., Jones, T.J., Harvey, P.M., Wilking, B.A., Joy, M., *The Astrophysical Journal*, 314, 283-296

Verma, R.P., Bisht, R.S., Ghosh, S.K., Iyengar, K.V.K., Rengarajan, T.N., Tandon, S.N., 1994, *Astronomy and Astrophysics*, 284, 936

Whiteoak, J.B., Gardner, F.F., 1974, *Astr. Ap.*, 37, 389

Whiteoak, J.B., Otrupcek, R.E., Rennie C.J., 1982, *Proc. Astr. Soc. Australia*, 4, 434

Wilson, T.L., Metxger, P.G., Gardner, F.F., Milne, D.K., 1970, *Astr. Ap.*, 6, 364

Wolk, S.J., Bourke, T.L., Smith, R.K., Spitzbart, B., Alves, J., 2002, *The Astrophysical Journal*, 580:L161-L165

This manuscript was prepared with the AAS LaTeX macros v5.0.